

Herschel observations of EXtra-Ordinary Sources (HEXOS): Observations of H₂O and its isotopologues towards Orion KL[★]

G. J. Melnick,¹ V. Tolls,¹ D. A. Neufeld,² E. A. Bergin,³ T. G. Phillips,⁴ S. Wang,³ N. R. Crockett,³ T. A. Bell,⁴ G.A. Blake,⁵ S. Cabrit,²³ E. Caux,^{6,7} C. Ceccarelli,⁸ J. Cernicharo,⁹ C. Comito,¹⁰ F. Daniel,^{9,11} M.-L. Dubernet,^{12,13} M. Emprechtinger,⁴ P. Encrenaz,¹¹ E. Falgarone,¹¹ M. Gerin,¹¹ T. F. Giesen,¹⁴ J. R. Goicoechea,⁹ P. F. Goldsmith,¹⁵ E. Herbst,¹⁶ C. Joblin,^{4,5} D. Johnstone,¹⁷ W. D. Langer,¹⁵ W.D. Latter,¹⁸ D. C. Lis,⁴ S. D. Lord,¹⁸ S. Maret,⁸ P. G. Martin,¹⁹ K. M. Menten,¹⁰ P. Morris,¹⁸ H. S. P. Müller,¹⁴ J. A. Murphy,²⁰ V. Ossenkopf,^{14,21} L. Pagani,²³ J. C. Pearson,¹⁵ M. Pérault,¹¹ R. Plume,²² S.-L. Qin,¹⁴ M. Salez,²³ P. Schilke,^{10,14} S. Schlemmer,¹⁴ J. Stutzki,¹⁴ N. Trappe,²⁰ F. F. S. van der Tak,²¹ C. Vastel,^{6,7} H. W. Yorke,¹⁵ S. Yu,¹⁵ and J. Zmuidzinas,⁴

(Affiliations can be found after the references)

Preprint online version: June 18, 2013

ABSTRACT

We report the detection of more than 48 velocity-resolved ground rotational state transitions of H₂¹⁶O, H₂¹⁸O, and H₂¹⁷O – most for the first time – in both emission and absorption toward Orion KL using *Herschel*/HIFI. We show that a simple fit, constrained to match the known emission and absorption components along the line of sight, is in excellent agreement with the spectral profiles of all the water lines. Using the measured H₂¹⁸O line fluxes, which are less affected by line opacity than their H₂¹⁶O counterparts, and an escape probability method, the column densities of H₂¹⁸O associated with each emission component are derived. We infer total water abundances of 7.4×10^{-5} , 1.0×10^{-5} , and 1.6×10^{-5} for the plateau, hot core, and extended warm gas, respectively. In the case of the plateau, this value is consistent with previous measures of the Orion-KL water abundance as well as those of other molecular outflows. In the case of the hot core and extended warm gas, these values are somewhat higher than water abundances derived for other quiescent clouds, suggesting that these regions are likely experiencing enhanced water-ice sublimation from (and reduced freeze-out onto) grain surfaces due to the warmer dust in these sources.

Key words. ISM: abundances — ISM: molecules

1. Introduction

During its 6-year mission, the Submillimeter Wave Astronomy Satellite (SWAS) surveyed more than 300 galactic sources and more than 6800 lines-of-sight (Melnick et al. 2000a), yet none produced stronger water emission than the line of sight toward Orion-KL. The source of this emission was attributed primarily to the chemistry and excitation accompanying the exceptionally powerful outflows emanating from the BN/KL region (Harwit et al. 1998; Wright et al. 2000; Melnick et al. 2000b; Cernicharo et al. 2006; Lerate et al. 2006); however, many sources possessing physical conditions favorable to the production of strong water emission – e.g. high densities and temperatures – are known to exist close to KL and could very likely be significant contributors to the water emission detected by ISO, SWAS, and *Odin*. Unfortunately, with access to only the ground-state $1_{10} - 1_{01}$ transition of ortho-H₂¹⁶O¹ and H₂¹⁸O, even the velocity-resolved SWAS and *Odin* measurements were limited in what could be inferred about the various components giving rise to the strong water emission.

The availability of the *Herschel*/HIFI instrument (deGraauw et al. 2010) with its extended frequency coverage and higher angular resolution, now permits a more detailed examination of the conditions responsible for the water emission toward Orion-KL.

Here we report the detection of 21 H₂O, 15 H₂¹⁸O, and 12 H₂¹⁷O velocity-resolved lines toward this source obtained as part of the HEXOS program (Bergin et al. 2010).

In this paper, we present an analysis of the sources of the water emission based upon the lower-opacity lines of H₂¹⁸O. We also show that the approach taken in this analysis holds great promise when applied to the H₂O and H₂¹⁷O lines, which will be pursued in a future paper.

2. Observations and results

The HIFI observations presented here were carried out in March and April 2010 using the spectral scan dual beam switch (DBS) mode pointed towards Orion-KL $\alpha_{J2000} = 5^h 35^m 14.3^s$ and $\delta_{J2000} = -5^\circ 22' 33.7''$. All observations were obtained with a beamsize of $\sim (22 / \nu_{\text{THz}})''$ and reference beams approximately 3' east and west, which is roughly orthogonal to the orientation of the Orion molecular ridge (e.g., Ungerechts et al. 1997). However, water emission is extended in Orion (Snell et al. 2000) and the reference beam may contain some contamination from a narrow ($\Delta v \sim 3 - 5 \text{ km s}^{-1}$) component centered at $\sim 9 \text{ km s}^{-1}$. We utilized the wide band spectrometer providing a spectral resolution of 1.1 MHz over a 4 GHz IF bandwidth. The data presented here are from a range of HIFI bands obtained as part of the HEXOS program. These data were reduced and converted to single side band as described by (Bergin et al. 2010), with additional analysis performed at the CfA. In our study, we adopt a uniform main beam efficiency of 70%.

[★] *Herschel* is an ESA space observatory with science instruments provided by European-led Principal Investigator consortia and with important participation from NASA.

¹ Also referred to simply as H₂O

Because of flux differences between the H- and the V-polarizations, which are most likely due to the known pointing offset between the two beams, we use only the H-polarization data for our analysis. The spectra for all H₂O, H₂¹⁷O, and H₂¹⁸O lines were extracted from the more extended HEXOS spectral scan data using the JPL Spectral Line Catalog (Pickett et al. 1998) for identification. Finally, the continuum offset appropriate to each line was determined directly from emission-free spectral regions near each line.

Figures 1 and 2 show the spectra of H₂¹⁸O and H₂O plus H₂¹⁷O, respectively. These spectra span a broad range of excitation conditions, ranging in upper-level energies between 53 K and more than 1000 K. All spectra have been examined for severe blending using the CLASS-Weeds tool (Maret et al. 2010), the JPL Spectral Line Catalog, or visual evidence of non-smooth water line wings. Blended lines were excluded from the following analysis.

3. Analysis

The goals of the present effort are twofold: (1) isolate the components giving rise to the water emission we detect; and, (2) model these components in a way that best reproduces the measured line fluxes and profiles. To do this, we focus here on the observed H₂¹⁸O lines. These lines have been detected over a broad range of excitation conditions with high signal-to-noise ratios and are much less affected by optical depth effects than their H₂¹⁶O counterparts, making the analysis more straightforward. In addition, the ¹⁶O:¹⁸O ratio is well known (i.e., ~ 500) and not believed to vary significantly between sources, making the conversion from inferred H₂¹⁸O abundance to H₂¹⁶O abundance robust.

Step 1 – isolate the components: The lines exhibit complex profiles which we attribute to a combination of emission and absorption components along the line of sight. To isolate what we believe are the three predominant emission components within the HIFI beams – namely the plateau molecular outflow, the hot core, and an extended region of gas composed of the compact ridge plus the warmer, denser portion of the extended ridge near KL (cf. Blake et al. 1987) – we adopt a line-fitting strategy that fixes the well-established characteristics of these regions, such as their v_{LSR} , and, in some cases, the typical line width, and leaves as free fitting parameters such quantities as the line strengths.

In addition to the three emission components, we include the effects of absorption by foreground material in two distinct kinematic components: a narrow component near 7 km s⁻¹, and a broad component centered at an LSR velocity of -5.1 km s⁻¹. While the presence of these absorption components is clearly required to fit the observed water line profiles, particularly in the case of low-lying transitions of H₂¹⁶O, the existence of foreground absorbing material at these velocities has been independently confirmed by HIFI observations of HF (Phillips et al. 2010), OH⁺ and H₂O⁺ (Gupta et al. 2010), as well as CRIRES observations of the fundamental CO vibrational band (Beuther et al. 2010). The narrow component arises in quiescent gas, while the broad, blueshifted component represents outflowing material, presumably associated primarily with the Low Velocity Flow (Genzel & Stutzki 1989). For the lower-lying transitions, these absorption components account for pronounced asymmetries in the line shapes, as well as the absorption feature close to the systemic source velocity (although we note here that narrow line emission in the reference beam is potentially a contributor to this absorption feature observed in the very lowest transitions.) Even in the case of H₂¹⁸O, transitions to the

Table 1. Fixed and varied parameters in water-line fits

Source	Peak T_A^* (K)	v_{LSR} (km s ⁻¹)	FWHM (km s ⁻¹)
Plateau	Varied	+6.9	Varied
Hot Core	Varied	+5.2	10.0
Extended warm gas	Varied	+8.25	2 – 8 †
Narrow absorption	Varied	+6.88	6.70
Broad absorption	Varied	-5.1	30.0

† The FWHM was constrained to vary between only 2 and 8 km s⁻¹.

ground states of ortho- or para-H₂¹⁸O (i.e., $2_{12} - 1_{01}$, $1_{10} - 1_{01}$ and $1_{11} - 0_{00}$) are affected by foreground absorption. Indeed, in the $1_{11} - 0_{00}$ and $2_{12} - 1_{01}$ H₂¹⁸O transitions, where the continuum brightness temperature is greatest, the blueshifted absorption feature can cause the observed antenna temperature to dip below the continuum level.

Thus, fits to all lines were made using the expression:

$$\text{Fitted Line } (T_A^*) = \left(\text{Continuum Offset} + G_{\text{plat}} + G_{\text{hc}} + G_{\text{ewg}} \right) \times \text{Exp}[-(G_{\text{na}} + G_{\text{ba}})], \quad (1)$$

where G_{plat} , G_{hc} , G_{ewg} , G_{na} and G_{ba} are Gaussian components representing the plateau, hot core, extended warm gas, narrow absorbing feature, and broad absorbing feature, respectively. Table 1 provides the fit parameters fixed by previous measurements and those that were allowed to vary, unconstrained, in order to obtain the best fit to the line profiles.

Step 2 – model the H₂¹⁸O emission components: The results of Step 1 are a set of best-fit integrated intensities for each component and transition, including the absorption features, that sum to reproduce the line flux and profile for each ortho- and para-H₂¹⁸O line. In this paper, we focus on the emission components only; analysis of the physical conditions associated with the absorption components will be undertaken following the results of a soon-to-be-completed water map toward Orion-KL. To assess how the H₂¹⁸O line strengths constrain the water abundance in each component, the equilibrium level populations of all H₂O ortho and para rotational levels of the ground vibrational state with energies E/k up to 2000 K have been calculated using an escape probability method that includes the necessary effects of radiative excitations due to dust emission embedded within each component. It is assumed that the water molecules see 4π steradians of dust emission from within each component. The velocity gradient for each transition is assumed to be equal to $\Delta v n(\text{H}_2)/N(\text{H}_2)$, where the line width, Δv , for each line for each component is taken from the best fit in Step 1, and $n(\text{H}_2)$ and $N(\text{H}_2)$ are the volume and column densities of H₂, respectively. The rate coefficients for collisions between ortho- and para-H₂ and ortho- and para-H₂O calculated by Faure et al. (2007) are used, and the H₂ ortho-to-para ratio is assumed to be the LTE value at the gas temperature of each component. Finally, the calculations incorporate the beam size and aperture efficiency appropriate to each transition.

More than 90% of the presently observed H₂O total line flux (and > 98% of the H₂¹⁸O and H₂¹⁷O total line flux) lies in transitions with $E_{\text{upper}} \leq 600$ K. Thus, we focus our modeling efforts primarily on reproducing the flux and profiles for these transitions. The H₂ density, gas and dust temperatures, source size, and ortho- and para-H₂¹⁸O column densities were varied to best match the inferred line fluxes for each emission component. The values yielding the best fit to the data are provided in Table 2.

Table 2. Best-fit radiative transfer model parameters for Orion H₂¹⁸O emission components

Source	Δv (km s ⁻¹)	T_{gas} (K)	$n(\text{H}_2)$ (cm ⁻³)	T_{dust}^\dagger (K)	θ_{source}	$N(\text{ortho/para-H}_2^{18}\text{O})$ (cm ⁻²)	Total Inferred H ₂ O Abundance [‡]
Extended warm gas	2–8	75	2×10 ⁶	30	20''	7.4×10 ¹⁵ (ortho) / 2.0×10 ¹⁵ (para)	1.6×10 ⁻⁵
Plateau	20–34	188	2×10 ⁶	113.6	24''	1.2×10 ¹⁶ (ortho) / 2.8×10 ¹⁵ (para)	7.4×10 ⁻⁵
Hot core	10	150	1×10 ⁷	180	5''	1.5×10 ¹⁶ (ortho) / 5.0×10 ¹⁵ (para)	1.0×10 ⁻⁵

[†] Greybody fit to the Orion continuum of the form: $B_{\tilde{\nu}}(T_{\text{dust}}) \times (0.0233 \tilde{\nu})^{0.486}$, where $\tilde{\nu}$ is wavelength in wavenumbers. [‡] Assumes ¹⁶O/¹⁸O = 500 and $N(\text{H}_2) = 3 \times 10^{23}$, 1×10^{23} , and 1×10^{24} cm⁻² in a 30'' beam for the extended ridge, plateau, and hot core, respectively (Blake et al. 1987).

The line profiles resulting from the radiative transfer model calculations for the emission components and Step 1 line-fits to the absorption components are shown as the red curves superposed on the observed spectra in Fig. 1. The models summarized in Table 2 provide a remarkably good match to the data, though the deviation between the models and the observed spectra for the higher-energy H₂¹⁸O transitions clearly illustrates the shortcomings of single-value models for each component as small amounts of hotter gas are not accounted for.

The physical conditions summarized in Table 2 have also been used to model the H₂¹⁶O lines with $E_{\text{upper}} \leq 400$ K. To do so, the column densities of ortho- and para-H₂¹⁶O are assumed to be 500 times greater than those of H₂¹⁸O, the line fluxes calculated, and then applied using the best-fit H₂¹⁶O plateau line widths determined using Eqn. 1. For the hot core and extended warm gas region, the H₂¹⁶O widths were assumed to be twice those of the H₂¹⁸O, and the absorption components are unchanged. The results of this simple approach are shown as the superposed red curves on the relevant H₂¹⁶O spectra in Fig. 2. The potential for a more careful analysis of the H₂¹⁶O and H₂¹⁷O lines is illustrated by how well the constrained fits match the other line profiles, shown as the superposed brown curves in Fig. 2. A more detailed model will be presented in a future paper.

4. Discussion

Modeling of the rich spectrum of H₂¹⁸O lines toward Orion-KL reveals several things. First, the relatively high H₂O abundance associated with the plateau is consistent with elevated water abundances measured previously toward KL (cf. Cernicharo et al. 2006) as well as toward a number of other molecular outflows (cf. Franklin et al. 2008). This is most likely the result of a combination of H₂O-ice sublimated and sputtered from grain surfaces and H₂O formed efficiently in the gas phase via neutral-neutral reactions favored in hotter portions of the plateau. The inferred water abundance for the plateau given in Table 2 is less than that cited in some larger-beamsize studies (e.g., Harwit et al. 1998, Melnick et al. 2000b), and may be due to the exclusion of more extended regions where the outflows encounter the surrounding quiescent material (cf. Genzel & Stutzki 1989). These shock-heated regions, which are particularly prominent in H₂ emission, can subject virtually all of the affected gas to temperatures in excess 1000 K, thus facilitating the neutral-neutral reactions that efficiently produce H₂O.

Second, the water abundances inferred for the hot core and extended warm gas are more than an order of magnitude greater than that inferred toward other quiescent regions (cf. Melnick & Bergin 2005). This is likely the result of enhanced sublimation of water-ice from, and reduced freeze-out onto, the warm dust grains present within both regions. It should be noted that the

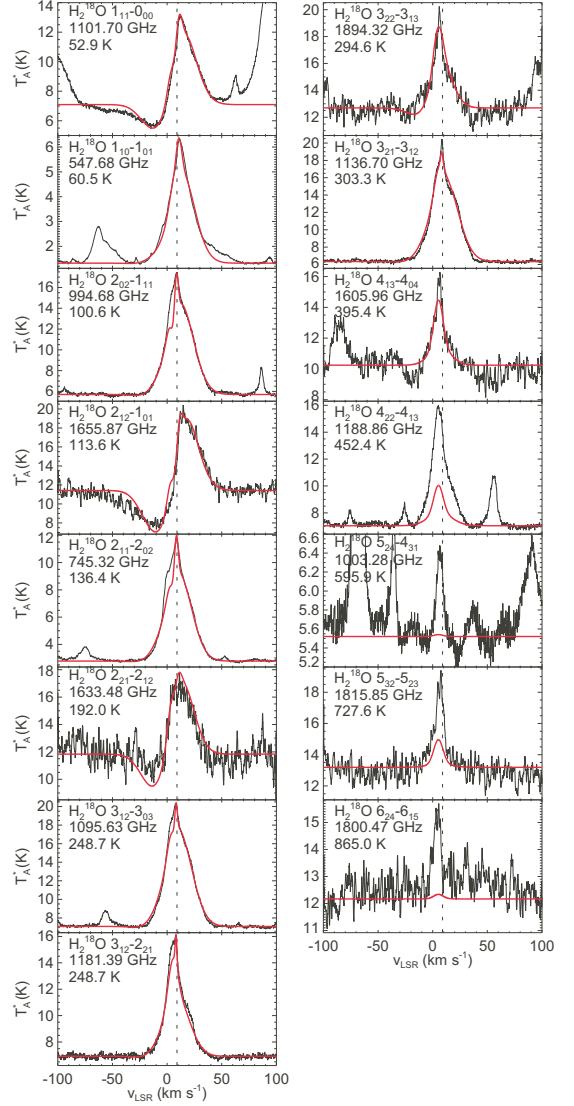


Fig. 1. H₂¹⁸O lines toward Orion-KL in order of increasing upper level energy. The superposed red curves show the line profiles resulting from our radiative transfer modeling of the emission components and line fits to the absorption components. The labels in the upper left corner of each plot list the species, the transition, the transition rest frequency, and the upper-level energy. The vertical dashed line denotes the 9 km s⁻¹ systemic velocity of the cloud. The 2₂₀–2₁₁, 4₂₃–3₃₀, 6₃₄–5₄₁, and 6₃₃–5₄₂ spectra are omitted due to blending with other lines or a low signal-to-noise ratio. We also note possible blending of the 4₂₂–4₁₃ line with CH₃OH (12₅₁–11₂₁) and H₂¹³CO (18₂₁₇–18₀₁₈), both of which lie within 27 km s⁻¹ of the H₂¹⁸O line.

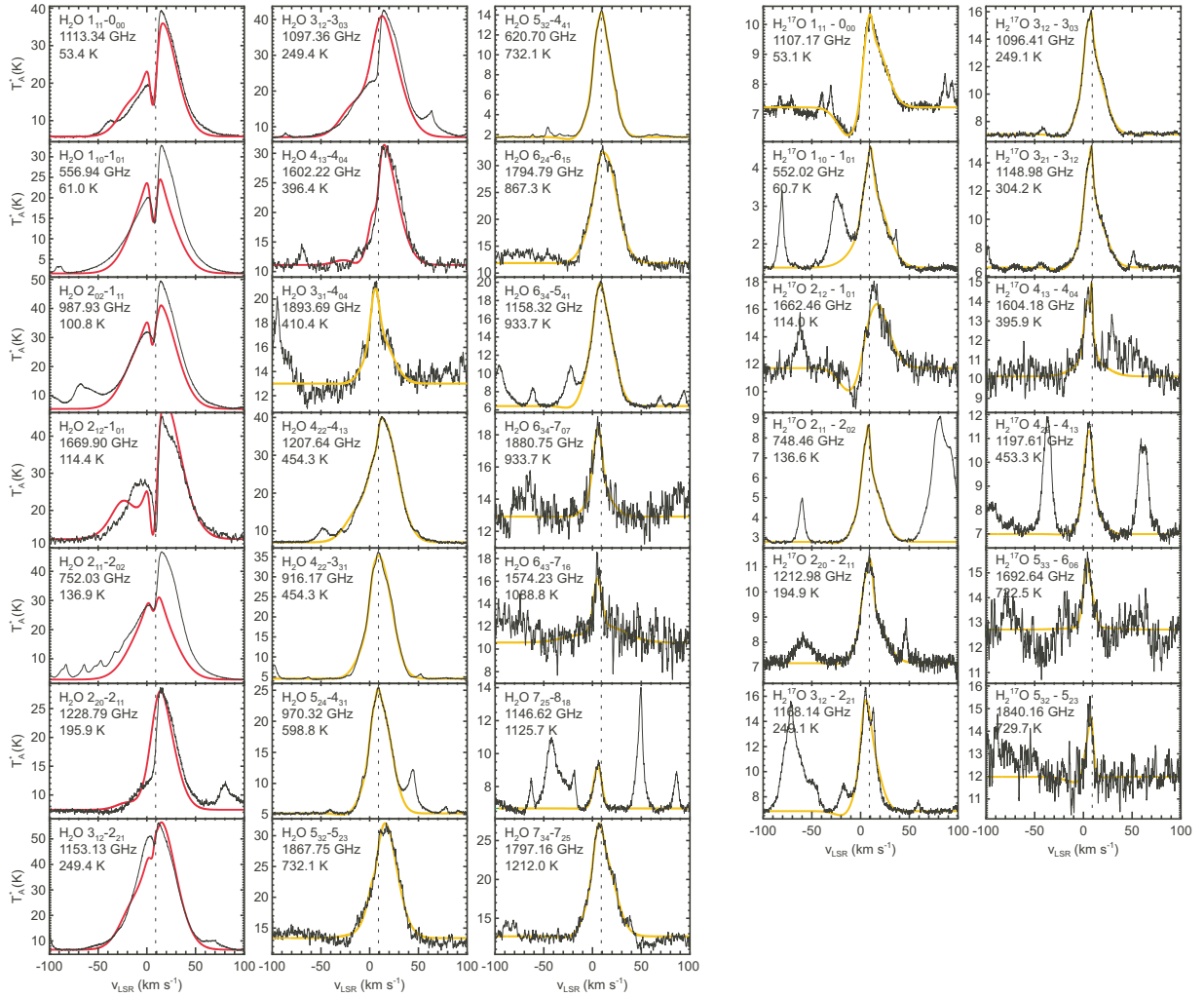


Fig. 2. *Left:* Same as Fig. 1, except showing the H_2^{16}O spectra toward Orion-KL/Hot Core in order of increasing upper level energy. The red curves superposed on the H_2^{16}O spectra with upper-level energies less than 400 K result from our radiative transfer model of the emission components and line fits to the absorption components. The brown curves show the best 5-component fit resulting from the procedure described in Section 3. The $2_{21} - 2_{12}$, $3_{21} - 3_{12}$, $6_{24} - 7_{17}$, $7_{34} - 7_{25}$, and $7_{44} - 6_{51}$ spectra have been omitted due to blending with other lines or a low signal-to-noise ratio. *Right:* H_2^{17}O spectra. The brown curves superposed on the spectra show the best 5-component fit resulting from the procedure described in Section 3. The $2_{02} - 1_{11}$ and $2_{21} - 2_{12}$ spectra have been omitted due to blending with other lines or a low signal-to-noise ratio.

gas and dust temperatures inferred for the extended warm gas should be viewed as lower limits given the probable presence of both water-line and continuum emission in the reference beam.

Finally, the H_2^{18}O ortho-to-para ratio inferred for all three emission components is consistent with a ratio of 3:1. A ratio of greater than 3:1 is likely the consequence of the rather simple model adopted for each component or residual inaccuracies in the water collisional rate coefficients, or both.

Acknowledgements. HIFI has been designed and built by a consortium of institutes and university departments from across Europe, Canada and the United States under the leadership of SRON Netherlands Institute for Space Research, Groningen, The Netherlands and with major contributions from Germany, France and the US. Consortium members are: Canada: CSA, U.Waterloo; France: CESR, LAB, LERMA, IRAM; Germany: KOSMA, MPIfR, MPS; Ireland, NUI Maynooth; Italy: ASI, IFSI-INAF, Osservatorio Astrofisico di Arcetri-INAF; Netherlands: SRON, TUD; Poland: CAMK, CBK; Spain: Observatorio Astronómico Nacional (IGN), Centro de Astrobiología (CSIC-INTA). Sweden: Chalmers University of Technology - MC2, RSS & GARD; Onsala Space Observatory; Swedish National Space Board, Stockholm University - Stockholm Observatory; Switzerland: ETH Zurich, FHNW; USA: Caltech, JPL, NHSC. Support for this work was provided by NASA through

an award issued by JPL/Caltech. CSO is supported by the NSF, award AST-0540882.

References

- Bergin, E.A., Phillips, T.G., Comito, C. et al. this volume
 Beuther, H., Linz, H., Bik, A., Goto, M., & Henning, T. 2010, *A&A*, 512, A29
 Blake, G. A., Sutton, E. C., Masson, C.R., & Phillips, T. G. 1987, *ApJ*, 315, 621
 Cernicharo, J., Goicoechea, J.R., Daniel, F. et al. 2006, *ApJ*, 649, L33
 Genzel, R. & Stutzki, J. 1989, *ARA&A*, 27, 41
 de Graauw, Th., Helmich, F.P., Phillips, T.G. et al., 2010, *A&A*, 518, L6
 Faure, A., Crimier, N., Ceccarelli, C., et al. 2007, *A&A*, 472, 1029
 Franklin, J., Snell, R.L., Kaufman, M.J. et al. 2008, *ApJ*, 674, 1015
 Gupta, H., Rimmer, P., Pearson, J.C. et al., this volume
 Harwit, M., Neufeld, D. A., Melnick, G. J., & Kaufman, M. J. 1998, *ApJ*, 497, L105
 Lerate, M. R., Barlow, M.J., Swinyard, B.M. et al. 2006, *MNRAS*, 370, 597
 Maret, S., Hily-Blant, P., Pety, J., Bardeau, S., and Reynier, E., in prep. (2010)
 Melnick, G. J., Stauffer, J.R., Ashby, M.L.N. et al. 2000a, *ApJ*, 539, L77
 Melnick, G. J., Ashby, M.L.N., Plume, R. et al. 2000b, *ApJ*, 539, L87
 Melnick, G. J. & Bergin, E. A. 2005, *Advances in Space Research*, 36, 1027
 Phillips, T.G., Bergin, E.A., Lis, D.C. et al. 2010, *A&A*, 518, L109

Pickett, H. M., Poynter, R. L., Cohen, E. A., et al. 1998, *J. Quant. Spectrosc. Radiat. Transfer*, 60, 883
 Pilbratt, G.L., Riedinger, J.R., Passvogel, T. et al. 2010, *A&A*, L1
 Snell, R. L., Howe, J.E., Ashby, M.L.N. et al. 2000, *ApJ*, 539, L93
 Ungerechts, H., Bergin, E.A., Goldsmith, P.F. et al. 1997, *ApJ*, 482, 245
 Wright, C.M., van Dishoeck, E.F., Black, J.H. et al. 2000, *A&A*, 358, 689

-
- ¹ Harvard-Smithsonian Center for Astrophysics (CfA), 60 Garden Street, Cambridge MA 02138, USA
e-mail: gmelnick@cfa.harvard.edu
 - ² Department of Physics and Astronomy, Johns Hopkins University, 3400 North Charles Street, Baltimore, MD 21218, USA
 - ³ Department of Astronomy, University of Michigan, 500 Church Street, Ann Arbor, MI 48109, USA
 - ⁴ California Institute of Technology, Cahill Center for Astronomy and Astrophysics 301-17, Pasadena, CA 91125 USA
 - ⁵ California Institute of Technology, Division of Geological and Planetary Sciences, MS 150-21, Pasadena, CA 91125, USA
 - ⁶ Centre d'étude Spatiale des Rayonnements, Université de Toulouse [UPS], 31062 Toulouse Cedex 9, France
 - ⁷ CNRS/INSU, UMR 5187, 9 avenue du Colonel Roche, 31028 Toulouse Cedex 4, France
 - ⁸ Laboratoire d'Astrophysique de l'Observatoire de Grenoble, BP 53, 38041 Grenoble, Cedex 9, France.
 - ⁹ Centro de Astrobiología (CSIC/INTA), Laboratorio de Astrofísica Molecular, Ctra. de Torrejón a Ajalvir, km 4 28850, Torrejón de Ardoz, Madrid, Spain
 - ¹⁰ Max-Planck-Institut für Radioastronomie, Auf dem Hügel 69, 53121 Bonn, Germany
 - ¹¹ LERMA, CNRS UMR8112, Observatoire de Paris and École Normale Supérieure, 24 Rue Lhomond, 75231 Paris Cedex 05, France
 - ¹² LPMAA, UMR7092, Université Pierre et Marie Curie, Paris, France
 - ¹³ LUTH, UMR8102, Observatoire de Paris, Meudon, France
 - ¹⁴ I. Physikalisches Institut, Universität zu Köln, Zùlpicher Str. 77, 50937 Köln, Germany
 - ¹⁵ Jet Propulsion Laboratory, Caltech, Pasadena, CA 91109, USA
 - ¹⁶ Departments of Physics, Astronomy and Chemistry, Ohio State University, Columbus, OH 43210, USA
 - ¹⁷ National Research Council Canada, Herzberg Institute of Astrophysics, 5071 West Saanich Road, Victoria, BC V9E 2E7, Canada
 - ¹⁸ Infrared Processing and Analysis Center, California Institute of Technology, MS 100-22, Pasadena, CA 91125
 - ¹⁹ Canadian Institute for Theoretical Astrophysics, University of Toronto, 60 St George St, Toronto, ON M5S 3H8, Canada
 - ²⁰ National University of Ireland Maynooth, Ireland
 - ²¹ SRON Netherlands Institute for Space Research, PO Box 800, 9700 AV, Groningen, The Netherlands
 - ²² Department of Physics and Astronomy, University of Calgary, 2500 University Drive NW, Calgary, AB T2N 1N4, Canada
 - ²³ LERMA & UMR8112 du CNRS, Observatoire de Paris, 61, Av. de l'Observatoire, 75014 Paris, France

Appendix

Table 3. Best-Fit H₂¹⁸O Integrated Line Intensities †

Transition	Frequency (GHz)	Upper-Level Energy (K)	Emission Component		
			Plateau $\int T_A^* dv$ (K-km s ⁻¹)	Hot Core $\int T_A^* dv$ (K-km s ⁻¹)	Extended Warm Gas $\int T_A^* dv$ (K-km s ⁻¹)
1 ₁₁ – 0 ₀₀	1101.70	52.9	315.4	7.6	50.8
1 ₁₀ – 1 ₀₁	547.68	60.5	199.0	8.2	34.6
2 ₀₂ – 1 ₁₁	994.68	100.6	423.3	60.1	10.7
2 ₁₂ – 1 ₀₁	1655.87	113.6	574.9	0.0	71.5
2 ₁₁ – 2 ₀₂	745.32	136.4	276.6	66.3	17.7
2 ₂₁ – 2 ₁₂	1633.48	192.0	220.6	10.1	6.4
3 ₁₂ – 3 ₀₃	1095.63	248.7	444.9	70.2	5.2
3 ₁₂ – 2 ₂₁	1181.39	248.7	178.8	50.4	1.8
3 ₂₂ – 3 ₁₃	1894.32	294.6	65.7	34.7	2.4
3 ₂₁ – 3 ₁₂	1136.70	303.3	424.4	65.3	11.8
4 ₁₃ – 4 ₀₄	1605.96	395.4	46.6	38.6	0.0
4 ₂₂ – 4 ₁₃ ^{††}	1188.86	452.4	118.5	57.5	0.2
5 ₂₄ – 4 ₃₁	1003.28	595.9	0.0	6.9	2.0
5 ₃₂ – 5 ₂₃	1815.85	727.6	22.2	32.8	10.0
6 ₂₄ – 6 ₁₅	1800.47	865.0	41.5	36.9	0.0

† The line fitting procedure is described in Section 3.

†† Some flux attributed to this transition may be due to the CH₃OH (12₅₁ – 11₂₁) and H₂¹³CO (18₂₁₇ – 18₀₁₈) transitions, both of which lie within 27 km s⁻¹ of the H₂¹⁸O 4₂₂ – 4₁₃ line.